Nano Research Energy

ISSN 2791-0091 CN 10-1944/O6
https://doi.org/10.26599/NRE.2026.9120295

Research Article

$CsBr/PbBr_2/CsBr$ sandwich-precursor deposition suppresses secondary phases in $CsPbBr_3$ solar cells

Wenhao Zhu[1,§], Minyue Zhang[1,§], Yang Wang[1,§], Chenwei Zhu[1], Yinuo Jin[1], Chunhong Zhang[1], Shaotian Chen[1], Shiying Sun[2,3], Yunjia Wu[1](✉), Chen Yang[2,3](✉), Weihai Sun[1](✉), Jihuai Wu[1](✉)

[1] Engineering Research Center of Environment-Friendly Functional Materials, Ministry of Education, College of Materials Science and Engineering, Huaqiao University, Xiamen 361021, China

[2] Research Center for Energy and Chemical Engineering, Xinjiang Technical Institute of Physics and Chemistry, Chinese Academy of Sciences, Urumqi 830011, China

[3] University of Chinese Academy of Sciences (UCAS), Beijing 100049, China

[§] Wenhao Zhu, Minyue Zhang and Yang Wang contributed equally to this work.

Nano Research Energy, **Just Accepted Manuscript** • https://doi.org/10.26599/NRE.2026.9120295
https://www.sciopen.com/journal/2791-0091 on Nov. 20, 2026

© The Authors(s)

Just Accepted

This is a "Just Accepted" manuscript, which has been examined by the peer-review process and has been accepted for publication. A "Just Accepted" manuscript is published online shortly after its acceptance, which is prior to technical editing and formatting and author proofing. Tsinghua University Press (TUP) provides "Just Accepted" as an optional and free service which allows authors to make their results available to the research community as soon as possible after acceptance. After a manuscript has been technically edited and formatted, and the page proofs have been corrected, it will be removed from the "Just Accepted" web site and published officially with volume and article number (e.g., Nano Research Energy, 2025, 4, e9120191). Please note that technical editing may introduce minor changes to the manuscript text and/or graphics which may affect the content, and all legal disclaimers that apply to the journal pertain. In no event shall TUP be held responsible for errors or consequences arising from the use of any information contained in these "Just Accepted" manuscripts. To cite this manuscript please use its Digital Object Identifier (DOI®), which is identical for all formats of publication.

Just Accepted

TABLE OF CONTENTS (TOC)

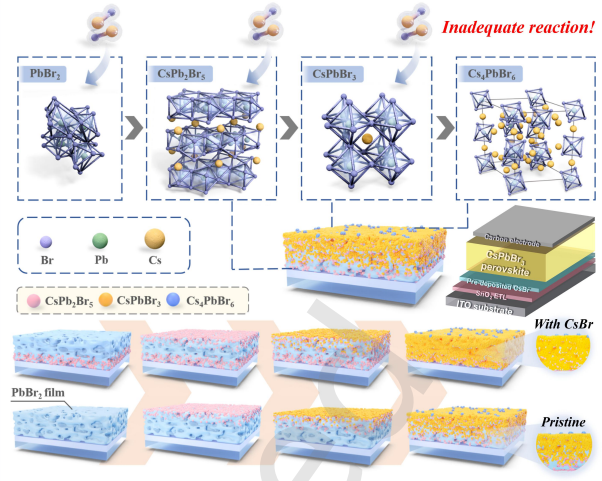
$CsBr/PbBr_2/CsBr$ sandwich-precursor deposition suppresses secondary phases in $CsPbBr_3$ solar cells

Wenhao Zhu[1,§], Minyue Zhang[1,§], Yang Wang[1,§], Chenwei Zhu[1], Yinuo Jin[1], Chunhong Zhang[1], Shaotian Chen[1], Shiying Sun[2,3], Yunjia Wu[1,*], Chen Yang[2,3,*], Weihai Sun[1,*], and Jihuai Wu[1,*]

[1] Engineering Research Center of Environment-Friendly Functional Materials, Ministry of Education, College of Materials Science and Engineering, Huaqiao University, China.

[2] Research Center for Energy and Chemical Engineering, Xinjiang Technical Institute of Physics and Chemistry, Chinese Academy of Sciences, China.

[3] University of Chinese Academy of Sciences (UCAS), China.



This work constructs a $CsBr/PbBr_2/CsBr$ sandwich precursor configuration by pre-depositing a CsBr underlayer onto SnO_2 prior to the deposition of $PbBr_2$, followed by a subsequent multistep CsBr conversion process.

The buried CsBr not only tailors the surface chemistry and energy-level alignment of SnO_2, but also promotes spatially homogeneous $CsPbBr_3$ conversion, effectively reducing harmful secondary phases.

Just Accepted

Nano Research Energy

ISSN 2791-0091 (print); 2790-8119 (online)
https://doi.org/10.26599/NRE.2026.9120295

Research Article

$CsBr/PbBr_2/CsBr$ sandwich-precursor deposition suppresses secondary phases in $CsPbBr_3$ solar cells

Wenhao Zhu[1,§], Minyue Zhang[1,§], Yang Wang[1,§], Chenwei Zhu[1], Yinuo Jin[1], Chunhong Zhang[1], Shaotian Chen[1], Shiying Sun[2,3], Yunjia Wu[1](✉), Chen Yang[2,3](✉), Weihai Sun[1](✉), and Jihuai Wu[1](✉)

[1] *Engineering Research Center of Environment-Friendly Functional Materials, Ministry of Education, College of Materials Science and Engineering, Huaqiao University, Xiamen 361021, China*
[2] *Research Center for Energy and Chemical Engineering, Xinjiang Technical Institute of Physics and Chemistry, Chinese Academy of Sciences, Urumqi, 830011, China*
[3] *University of Chinese Academy of Sciences (UCAS), Beijing, 100049, China*
[§] *Wenhao Zhu, Minyue Zhang and Yang Wang contributed equally to this work.*

Received: 31 August 2026 / **Revised:** 23 October 2026 / **Accepted:** 8 November 2026

ABSTRACT

Multistep conversion of all-inorganic $CsPbBr_3$ solar cells often produces lead-rich and cesium-rich secondary phases because CsBr penetrates $PbBr_2$ nonuniformly. Here, a $CsBr/PbBr_2/CsBr$ sandwich precursor is constructed by inserting a CsBr underlayer between SnO_2 and $PbBr_2$. The buried CsBr modifies $PbBr_2$ morphology, promotes more uniform phase conversion, and regulates the surface chemistry and energetics of SnO_2. The resulting films exhibit larger grains, a reduced $CsPb_2Br_5$ diffraction contribution, and lower Urbach energy. Hole-transport-layer-free carbon-electrode devices deliver a champion efficiency of 10.12% (V_{OC} = 1.57 V, J_{SC} = 7.98 mA·cm^{-2}, and FF = 80.74%), compared with 7.98% for control devices, together with a stabilized efficiency of 9.51% at 1.26 V. Unencapsulated devices retain over 80% of their initial efficiency after 1000 h under atmospheric storage. This sandwich-precursor strategy provides a simple route to regulate phase conversion and buried interfaces in $CsPbBr_3$ solar cells.

KEYWORDS

$CsPbBr_3$ solar cells; Sandwich precursor; Phase conversion; Buried interface; CsBr pre-deposition.

1 Introduction

Perovskite solar cells (PSCs) have emerged as a focal point of global research owing to their low manufacturing costs, exceptional performance, and tunable optical band gap[1–3]. Over the past decades, the power conversion efficiency (PCE) of PSCs has markedly increased from 3.8% to 28.0%, underscoring their huge potentials[4,5]. However, organic-inorganic hybrid perovskites remain vulnerable to environmental stresses such as moisture, oxygen, and heat, motivating the development of more robust all-inorganic absorbers[6]. Among them, $CsPbBr_3$ is particularly attractive because of its favorable thermal and phase stability, wide bandgap, and compatibility with hole-transport-layer-free carbon-electrode architectures[7–10]. Nevertheless, the efficiencies of $CsPbBr_3$ PSCs remain considerably below their theoretical limit of approximately 16.5%, mainly because of incomplete phase conversion, bulk and interfacial defects, and inefficient carrier extraction[10–12].

$CsPbBr_3$ films are commonly fabricated by multistep conversion because of the limited solubility of CsBr in conventional polar solvents[13]. In this process, a $PbBr_2$ precursor film is deposited first and subsequently converted through repeated coating with a CsBr solution. The conversion therefore proceeds predominantly from the exposed surface toward the buried interface. Limited penetration of CsBr through compact $PbBr_2$ films can produce a vertically nonuniform Cs distribution and leave lead-rich intermediate or secondary phases near the bottom of the perovskite layer. These residual phases disrupt the continuity of the $CsPbBr_3$ lattice and introduce recombination-active regions[14,15]. Meanwhile, the buried interface is formed directly on the electron transport layer (ETL), where oxygen-vacancy-related defects and unfavorable energy-level offsets in SnO_2 can

© The Author(s) 2026. Published by Tsinghua University Press. The articles published in this open access journal are distributed under the terms of the Creative Commons Attribution 4.0 International License (http://creativecommons.org/licenses/by/4.0/), which permits use, distribution and reproduction in any medium, provided the original work is properly cited.

Address correspondence to Jihuai Wu, jhwu@hqu.edu.cn; Weihai Sun, sunweihai@hqu.edu.cn; Chen Yang, yangchen@ms.xjb.ac.cn; Yunjia Wu, wuyunjia@stu.hqu.edu.cn

Just Accepted

further promote interfacial charge accumulation and nonradiative recombination[16]. Consequently, precursor conversion and buried-interface quality are closely coupled during multistep $CsPbBr_3$ deposition[17–19].

Previous studies have demonstrated the importance of regulating either precursor conversion or the buried electron-transport interface. Li et al. modified TiO_2 ETL with methylammonium chloride to enhance electron extraction and suppress interface recombination, resulting in an increase of PCE from 8.42 % to 10.10 %[20]. Zhang et al. introduced a sandwich structure strategy utilizing MAI-PbI_2-MAI to alleviate the detrimental effects of residual PbI_2 during the two-step deposition process[21]. Additionally, Xiao et al. further modified the SnO_2 film using methylene diammonium dichloride o reduce surface defects and improve energy-level alignment[22]. These studies show that spatial precursor design and buried-interface modification can each improve perovskite formation and carrier transport.

In this work, we construct a $CsBr/PbBr_2/CsBr$ sandwich precursor configuration by pre-depositing a CsBr underlayer on SnO_2 before the deposition of $PbBr_2$ and the subsequent multistep CsBr conversion. The buried CsBr not only alters the surface chemical environment and energy-level structure of SnO_2, but also promotes more spatially uniform conversion of $CsPbBr_3$, thereby reducing detrimental secondary phases (Pb-rich and Cs-rich). The resulting $CsPbBr_3$ films exhibit enlarged grains, reduced energetic disorder, and suppressed nonradiative recombination. Hole-transport-layer-free carbon-electrode devices based on this strategy achieve a champion PCE of 10.12%, compared with 7.98% for the control devices, together with a stabilized efficiency of 9.51%. This work establishes sandwich-precursor engineering as a simple strategy for coordinating phase conversion and buried-interface regulation in $CsPbBr_3$ PSCs.

2 Experimental

Materials: Indium-tin oxide conductive glass (ITO, 7 Ω sq^{-1}), cesium bromide (CsBr, 99.999%) and lead bromide ($PbBr_2$, 99.99%) were provided by Advanced Election Technology Co., Ltd. 15% SnO_2 colloidal solution was supplied by Alfa Aesar Co., Ltd and stored in refrigerator in dark condition. Methanol (CH_3OH, AR) was purchased from Shanghai Sinopharm Group Chemical Reagent Co., Ltd. N,N-dimethylformamide (DMF, 99.8%) and dimethyl sulfoxide (DMSO, 99.7%) were provided by J&K Scientific. Carbon paste was acquired from Shanghai Mater Win New Materials Co., Ltd. All materials were used as received without further purification.

Fabrication of PSCs: The ITO glass underwent sequential treatment with deionized (DI) water, ethanol, and ultraviolet ozone for 20 min each. A SnO_2 colloidal solution was prepared by mixing SnO_2 with deionized water in a volume ratio of 1:4, followed by treatment in an ultrasonic cleaner for 20 min while maintained in an ice bath. A volume of 70 μL of the dispersed SnO_2 solution was spin-coated onto the pretreated ITO glass at 3500 rpm for 25 s and subsequently annealed at 180 ℃ for 30 min. Following this, the ITO glass with the SnO_2 electron transport layer (ETL) received a UV ozone cleaning treatment for 20 min. For experimental devices, the SnO_2 ETL was spin-coated with 120 μL of a CsBr solution, which was dissolved in methanol at a concentration of 0.07 M, at 2000 rpm for 30 s. The coated layer was then heated at 50 ℃ for 10 min before the spin-coating of a $PbBr_2$ solution, which was dissolved in DMF at a concentration of 1 M. Subsequently, 120 μL of the $PbBr_2$ solution was spin-coated onto the previously formed films under the same parameters of 2000 rpm for 30 s and annealed at 100 ℃ for 30 min to facilitate crystal formation and the evaporation of DMF solvent. Notably, the experimental devices employed three different annealing temperatures of 100 ℃, 150 ℃, and 200 ℃ to form the thin films. Subsequently, 120 μL of CsBr solution was spin-coated onto a cooled $PbBr_2$ film under identical parameters, followed by annealing at 250 °C for 5 min. This process was repeated eight times to create a $CsPbBr_3$ perovskite film. Finally, a cotton swab dipped in an erasing solution (DMSO and methanol mixed in a volume ratio of 9:1) was used to erase an appropriate width on one side of the vertical conductive layer. Carbon electrodes were then applied to the perovskite layer through screen printing and underwent a 15 min annealing at 120 °C to yield a complete $CsPbBr_3$ perovskite solar cell.

Characterization: Surface topography was acquired using cold-field emission scanning electron microscopy (FESEM, S4800). X-ray diffraction patterns were obtained through an X-ray powder diffractometer (Bruker AXS D8 advance) with Cu Kα radiation to characterize the crystal structure and phase of the thin films. X-ray photoelectron spectroscopy (XPS) and ultraviolet photoemission spectroscopy (UPS) experiments were conducted on the Escalab 250Xi, employing monochromatic Al-Kα radiation as the excitation source. The ultraviolet–visible (UV–vis) absorption spectrum was measured with a UV–vis spectrophotometer (Shimadzu, UV-2550) over a range of 300–850 nm. Steady-state photoluminescence (PL) and transient photoluminescence (TRPL) spectra were obtained using LF-1303003 and Omin-λ Monochromator/Spectrograph. Electrochemical impedance spectroscopy (EIS), transient photocurrent/photovoltage (TPC/TPV), capacitance-voltage (C-V), and Mott-Schottky (M-S) curves were measured with an electrochemical workstation (Zahner IM6e, Germany) in a dark environment. The *J-V* curves of the devices were recorded using a PVIV-94043A (Newport, USA) solar simulator, which provided AM 1.5 G 100 mW·cm^{-2} solar illumination and was calibrated with a standard monocrystalline silicon solar cell. The steady-state output curves were also measured with an electrochemical workstation (Zahner IM6e, Germany), while under the AM 1.5 G 100 mW·cm^{-2} solar illumination

Just Accepted

provided by PVIV-94043A (Newport, USA) solar simulator, which was calibrated with a standard monocrystalline silicon solar cell.

3 Results and discussion

3.1 Surface morphology of films with or without CsBr pre-deposition

Fig. 1a schematically illustrates the sandwich-precursor deposition processes, while the physical imagine of the device is presented in Fig. S1. As shown in Fig. S2, the SnO_2 film has no significant changes after CsBr pre-deposited. Compared with the pristine $PbBr_2$ film, the film deposited on the CsBr underlayer exhibits a more porous morphology (Figs. 1b, c). After conversion, the resulting $CsPbBr_3$ film shows a compact and pinhole-free surface, with the average grain size increasing from 645.3 to 1106.0 nm (Figs. 1d, e) and Fig. S3). Cross-sectional SEM images further revealed enlarged grains, fewer vertical grain boundaries, and an increased film thickness after CsBr pre-deposition (Figs. 1f, g). These morphological changes indicated that the buried CsBr layer promoted the growth of larger $CsPbBr_3$ grains, which were expected to suppress charge carrier recombination and improve the light absorption of $CsPbBr_3$ layer[23].

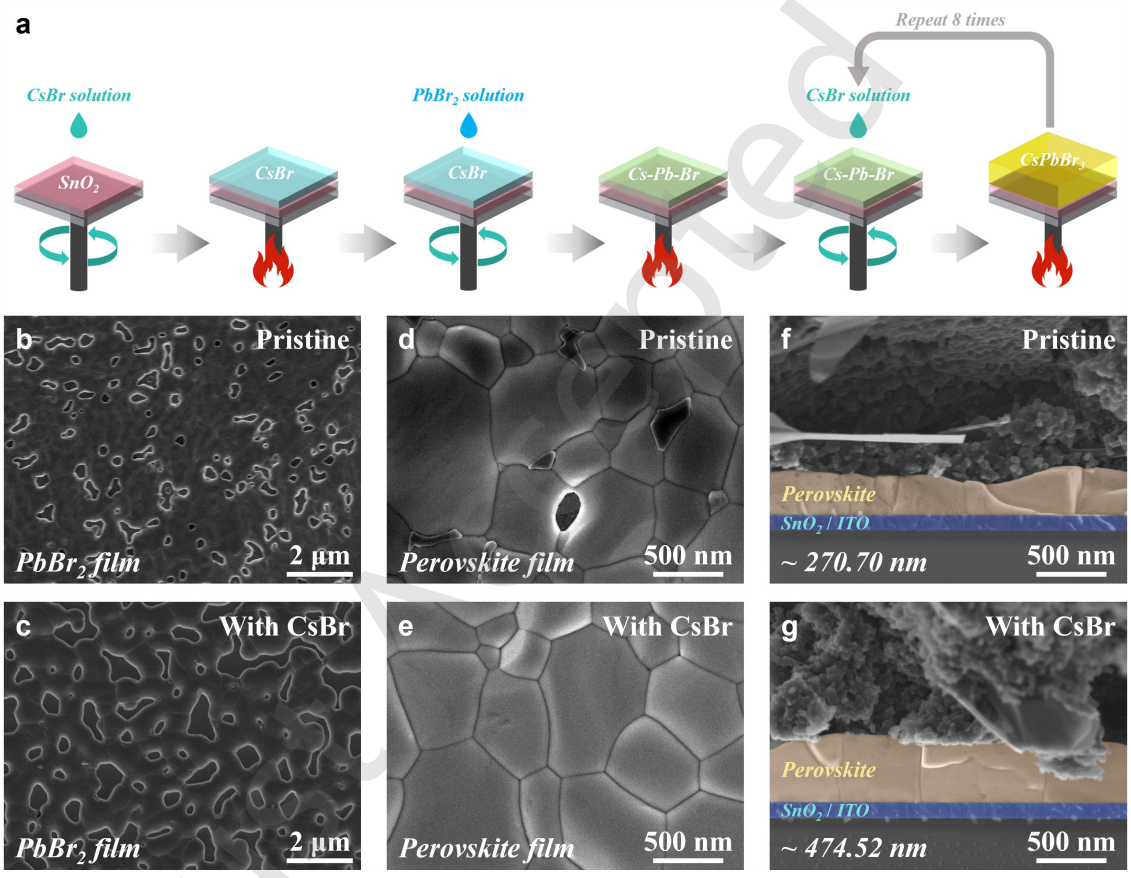


Figure 1 (a) Schematic illustration of sandwich-precursor deposition processes for PVK; SEM images of (b) pristine $PbBr_2$ films and (c) $PbBr_2$ films with CsBr; SEM images of (d) pristine PVK films and (e) PVK films with CsBr; Cross-sectional SEM images of (f) pristine devices and (g) devices with CsBr.

3.2 Phase analysis and optical properties of perovskite

The phase purity and crystallinity of $PbBr_2$ films and PVK films were analyzed by X-ray diffraction (XRD) before and after CsBr pre-deposition. In $PbBr_2$ films (Fig. 2a), diffraction peaks of $PbBr_2$ with crystal planes of (020), (120), and (012) appeared at diffraction angles of 18.5°, 22.0°, and 37.6°, respectively[24]. After CsBr pre-deposition, a decrease in diffraction intensity at (020) and (012) crystal planes was observed, accompanied by the emergence of a new peak at 11.6° corresponding to the (002) plane of $CsPb_2Br_5$ [25]. The emergence of $CsPb_2Br_5$ indicates that the pre-deposited CsBr reacts with the overlying $PbBr_2$ precursor, initiating phase conversion before the subsequent CsBr coating. The introduction of a small amount of CsBr has changed the highly crystalline morphology of the original $PbBr_2$, promoting the formation of the low-order $CsPb_2Br_5$ phase and resulting in a porous structure in the $PbBr_2$ film[25]. Additionally, Fig. 2b presented the XRD patterns of the PVK films with and without the introduction of CsBr, along with the corresponding enlarged images in Fig. 2c. After CsBr pre-deposition, the $CsPbBr_3$ reflections at 15.2°, 21.6°, 30.7°, and 37.8°, assigned to the (100), (110), (200), and (211) planes, respectively, become more pronounced[26]. In contrast, the $CsPb_2Br_5$ (005) reflection at 29.4° decreased. These changes are consistent with the enhanced conversion of the lead-rich $CsPb_2Br_5$ intermediate into $CsPbBr_3$ and a reduced contribution

from secondary phases, supporting more complete phase conversion through the sandwich-precursor process[27]. Additionally, the magnified XRD patterns of PVK in the range of 27°–33° have been presented in Fig. S4. The analysis has revealed a decrease in the diffraction intensities of the (005) and (233) crystal planes corresponding to $CsPb_2Br_5$ and Cs_4PbBr_6[28], indicating that the pre-deposition of CsBr has promoted the enhancement of phase purity.

Furthermore, Fig. 2d compared the ultraviolet–visible (UV–vis) absorption spectra of PVK films with or without CsBr pre-deposition. The film prepared with CsBr pre-deposition exhibits stronger absorption in the visible region, which likely arises from the combined effects of improved film coverage and increased thickness observed by SEM[29]. The optical bandgaps of the $CsPbBr_3$ films were estimated from the corresponding Tauc plots (Fig. S5a). Nearly identical values of 2.347 and 2.350 eV were obtained for the pristine and CsBr-predeposited films, respectively, confirming that the buried CsBr layer had a negligible influence on the intrinsic optical bandgap. To further evaluate band-edge disorder, the absorption-tail region was analyzed by extracting the Urbach energy (E_U) according to the following relationship[30]:

$$\alpha(E) = \alpha_0 e^{\frac{E-E_C}{E_U}} \#Eq.(1)$$

where α represented the absorption coefficient, E denoted the photon energy, and α_0 and E_C were material constants. As shown in Fig. S5b, CsBr pre-deposition reduced the E_U from 57.32 to 44.65 meV. The lower E_U reflects a sharper absorption edge and diminished energetic disorder, consistent with a reduced density of sub-bandgap tail states and improved optoelectronic quality of the $CsPbBr_3$ film[31]. Meanwhile, the UV–vis absorption spectra of SnO_2 layers were shown in Fig. S6a, and the corresponding Tauc plots were provided in Fig. S6b. The optical bandgap changes only marginally from 3.97 to 3.95 eV after CsBr pre-deposition, indicating that the CsBr underlayer does not appreciably alter the intrinsic optical band structure of SnO_2. Its influence on the interfacial energy-level alignment was examined in greater detail below using ultraviolet photoelectron spectroscopy.

Fig. 2e compared the steady-state photoluminescence (PL) spectra of the $CsPbBr_3$ films. The film prepared with CsBr pre-deposition exhibits stronger emission intensity, which, under identical measurement conditions, is consistent with a lower proportion of photogenerated carriers lost through nonradiative pathways[32]. This interpretation agrees with the reduced E_U discussed above. The corresponding time-resolved photoluminescence decay curves are displayed in Fig. 2f, with the fitted data detailed in Table S1. The carrier lifetime was evaluated by the biexponential decay function[33]:

$$I(t) = A_1 e^{\frac{-t}{\tau_1}} + A_2 e^{\frac{-t}{\tau_2}} + B \#Eq.(2)$$

where A_1 and A_2 represented crucial amplitudes for the fitting process, τ_1 denoted the fast decay lifetime associated with trap-assisted nonradiative recombination, and τ_2 signified the slower component linked to radiative recombination. The average lifetime of the PVK films increased from 7.50 ns to 10.20 ns following CsBr pre-deposition, indicating slower photoluminescence decay and diminished nonradiative recombination. Together, the steady-state and time-resolved photoluminescence results support the improved optoelectronic quality of the $CsPbBr_3$ film[34].

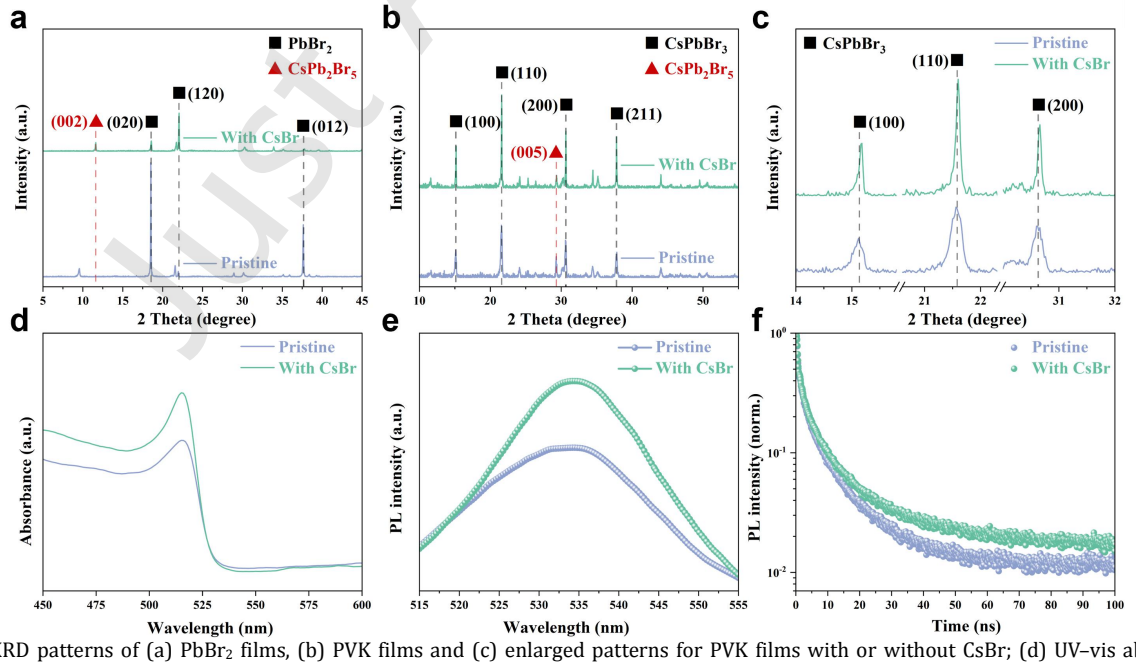


Figure 2 XRD patterns of (a) $PbBr_2$ films, (b) PVK films and (c) enlarged patterns for PVK films with or without CsBr; (d) UV–vis absorption spectra, (e) steady-state PL spectra and (f) TRPL spectra of PVK films with or without CsBr.

3.3 Chemical reconstruction and energy level adjustment of SnO_2/perovskite interface

To investigate the mechanism of CsBr pre-deposition in precursor conversion, X-ray photoelectron spectroscopy

Just Accepted

(XPS) was performed on $PbBr_2$ films. The corresponding survey spectra are compiled in Fig. S7a, while the high-resolution Cs 3d, Pb 4f, and Br 3d spectra were resolved in Figs. 3a–c. Following CsBr pre-deposition, the appearance of the Cs 3d signal and the concomitant binding-energy shifts of Pb 4f and Br 3d verify the introduction of Cs-containing species and their chemical interaction with $PbBr_2$[23]. In addition, the metallic Pb^0 component detected in the pristine $PbBr_2$ film is no longer discernible after CsBr pre-deposition. This change suggests that the reduction of Pb^{2+} to Pb^0 is suppressed, possibly because the early formation of the $CsPb_2Br_5$ intermediate stabilizes the Pb-containing precursor[35]. On this basis, the proposed conversion pathways for the conventional and sandwich-precursor processes were schematically compared in Fig. 3g, with the associated phase evolution in the CsBr-$PbBr_2$ system summarized in Fig. S8. The pre-deposition of CsBr has effectively enhanced the utilization of $PbBr_2$ at the bottom and has formed a porous $PbBr_2$ film. This process has promoted the complete reaction of CsBr, reduced the generation of the $CsPb_2Br_5$ phase within the film, and minimized the formation of the Cs_4PbBr_6 phase on the surface, thereby improving the overall phase purity of the PVK film. In addition to regulating precursor conversion, the buried CsBr layer modifies the chemical and electronic characteristics of the SnO_2/$CsPbBr_3$ interface. This interfacial effect was evaluated by combining XPS (full spectrum at Fig. S7b) with ultraviolet photoelectron spectroscopy (UPS). The emergence of Cs 3d and Br 3d signals on the CsBr-treated SnO_2 surface confirms the presence of CsBr-derived species at the buried interface (Figs. S7c, d). Meanwhile, both the Sn 3d and O 1s peaks shifted toward lower binding energies (Figs. S7e, f), pointing to a redistribution of electron density and an altered local coordination environment in SnO_2. These spectral variations are consistent with the interaction of Br^- with undercoordinated Sn sites and oxygen-vacancy-related defects, which may decrease the density of interfacial recombination centers[36,37].

The accompanying changes in the surface electronic structure were further examined by UPS. The complete UPS spectra were provided in Fig. S9, and the secondary-electron cutoff and valence-band onset regions were enlarged in Fig. 3d, e. With CsBr pre-deposition, the cutoff energy (E_{cutoff}) increased from 16.81 to 16.95 eV, corresponding to a reduction in the SnO_2 work function from 4.41 to 4.27 eV (Table S2). Concurrently, the conduction-band minima (E_{CB}) shifted from -3.99 to -3.95 eV after the incorporation of CsBr. As depicted in Fig. 3f, this energetic adjustment slightly reduces the conduction-band offset at the SnO_2/$CsPbBr_3$ interface while preserving favorable electron transfer. Collectively, the XPS and UPS results demonstrate that the buried CsBr layer not only alters the local chemical environment of SnO_2 but also optimizes its interfacial energetics, thereby potentially promoting electron extraction and mitigating interfacial energy losses[38].

3.4 Photovoltaic performance of devices

Fig. 4a depicted the device architecture employed in this study. To optimize the thermal treatment of the buried CsBr layer, devices based on pristine $CsPbBr_3$ films and CsBr-predeposited films annealed at different temperatures were fabricated and evaluated. Current density-voltage (*J-V*) tests have been conducted in reverse scan mode at ambiet air condition and a relative humidity of 25% under simulated sunlight, with an illuminated area of 0.0225 cm^2. As summarized in Fig. 4b and Table 1, the control device delivered a power conversion efficiency (PCE) of 7.98%, with an open-circuit voltage (V_{OC}) of 1.47 V, a short-circuit current density (J_{SC}) of 7.11 $mA{\cdot}cm^{-2}$, and a fill factor (FF) of 76.32%. The photovoltaic parameters exhibited a pronounced dependence on the annealing temperature of the CsBr underlayer, with the device performance improving progressively as the temperature increased to 150 °C. Under the optimized condition, the champion device attained a PCE of 10.12%, together with a V_{OC} of 1.57 V, a J_{SC} of 7.98 $mA{\cdot}cm^{-2}$, and an FF of 80.74%.

Table 1 Photovoltaic data of CsBr pre-deposited devices at different annealing temperatures.

Sample	V_{OC} (V)	J_{SC} ($mA{\cdot}cm^{-2}$)	FF (%)	PCE (%)
Pristine	1.47	7.11	76.32	7.98
100 °C	1.52	7.79	76.01	9.00
150 °C	1.57	7.98	80.74	10.12
200 °C	1.53	7.78	78.80	9.38

In light of the structural, optical, and spectroscopic analyses described above, this performance enhancement can be ascribed to the complementary functions of the buried CsBr layer. Specifically, CsBr regulates precursor conversion and promotes the formation of higher-quality $CsPbBr_3$ films while simultaneously modifying the surface chemistry and energy-level alignment of SnO_2. These effects reduce nonradiative recombination losses and establish a more favorable buried interface for electron extraction and transport. Beyond the optimal annealing temperature, however, the device efficiency declined markedly. This may result from excessive thermal treatment disturbing the coverage or interfacial distribution of CsBr.

The statistical distributions of the photovoltaic parameters obtained from 40 independently fabricated devices were displayed in Fig. 4c and Fig. S10. The control devices yielded an average PCE of 6.81% and exhibited a relatively broad efficiency distribution. By comparison, the CsBr-predeposited devices achieved a substantially higher average PCE of 9.18%, accompanied by a narrower distribution and a smaller standard deviation (Table S3). The simultaneous increase in average efficiency and reduction in device-to-device variation demonstrate that

Just accepted

the buried CsBr strategy enhances both photovoltaic performance and fabrication reproducibility.

To corroborate the photovoltaic performance derived from the *J-V* measurements, stabilized power-output measurements were conducted under continuous illumination for 400 s (Fig. 4d). At a fixed operating voltage of 1.26 V, the CsBr-predeposited device sustained a steady-state current density of 7.55 mA·cm^{-2}, corresponding to a stabilized PCE of 9.51%. Both values substantially exceed those of the control device and accord well with the performance trend obtained from the *J-V* curves, confirming the reliability of the efficiency enhancement achieved through CsBr pre-deposition.

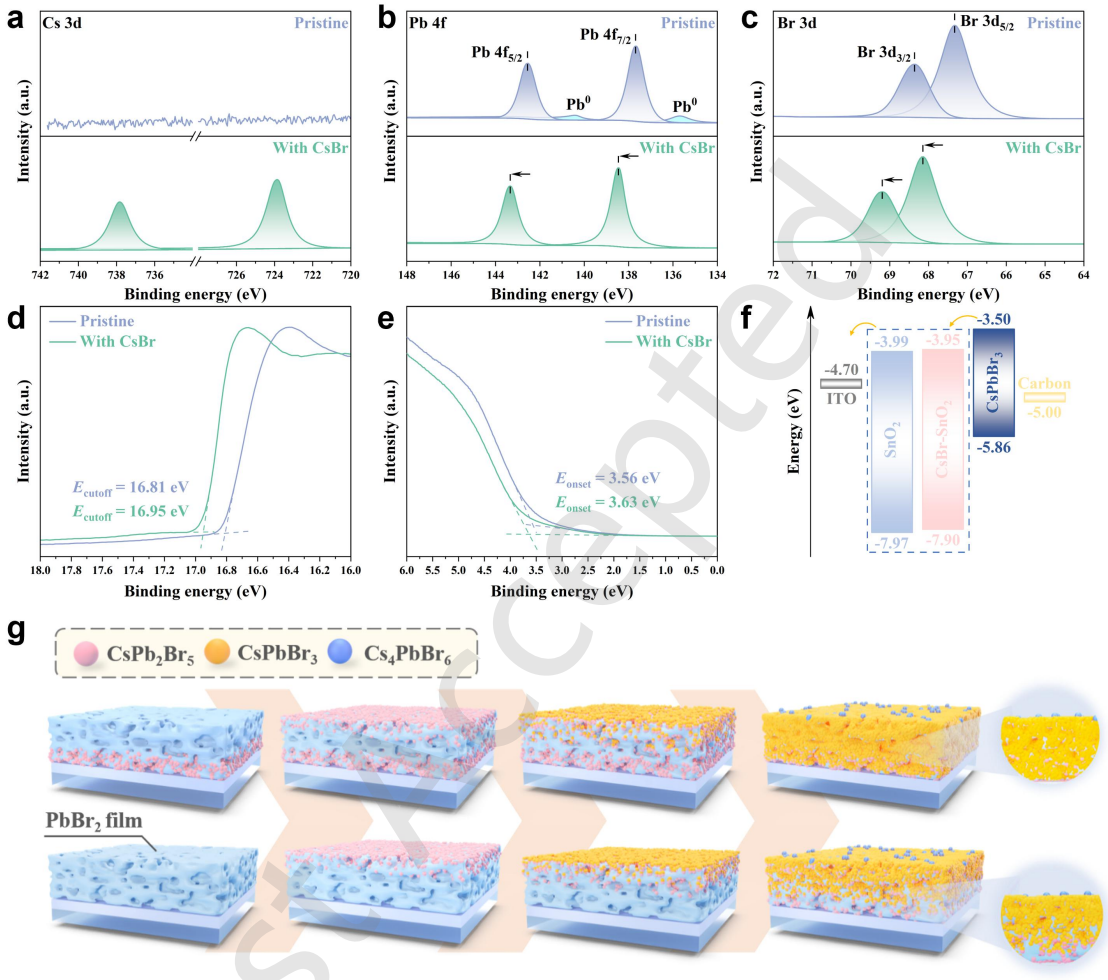


Figure 3 The corresponding high-resolution XPS spectra of (a) Cs 3d, (b) Pb 4f and (c) Br 3d for $PbBr_2$ films with or without CsBr; (d) The cutoff energy (E_{cutoff}) region and (e) the onset energy (E_{onset}) region for the SnO_2 films with or without CsBr; (f) Schematic diagram of energy levels at the buried interface; (g) The schematic diagram of the reaction mechanism of CsBr pre-deposition on SnO_2 films and highlights the role of CsBr in enhancing the phase purity of PVK.

Electrochemical impedance spectroscopy (EIS) was subsequently employed to probe the charge-transport and recombination kinetics within the devices. Fig. 4e displayed the Nyquist plots recorded under dark conditions, with the fitted parameters compiled in Table S4. Relative to the control device, the CsBr-predeposited device exhibited a reduction in series resistance (R_s) from 37.37 to 27.56 Ω, accompanied by an increase in recombination resistance (R_{rec}) from 802 to 1396 Ω. The lower R_s signifies diminished resistive losses, whereas the elevated R_{rec} reflects a stronger suppression of carrier recombination[39].

The impedance responses measured under one-sun illumination were presented in Fig. 4f. Two characteristic regions can be distinguished in the Nyquist plots, arising from the charge-transfer and recombination processes within the operating devices. As summarized in Table S5, CsBr pre-deposition decreased the charge-transfer resistance (R_{ct}) from 1464 to 768.3 Ω while increasing R_{rec} from 1832 to 3365 Ω. The pronounced reduction in R_{ct} indicates that the kinetic barrier to interfacial charge transfer is alleviated, whereas the higher R_{rec} points to reduced recombination under working conditions[40]. Both the dark and illuminated EIS measurements provide an electrical basis for the enhanced photovoltaic parameters: suppressed recombination contributes primarily to the higher V_{OC}, while reduced series and charge-transfer resistances facilitate the improvement in FF[41].

To quantify the trap-state density (N_t) in the $CsPbBr_3$

Just Accepted

films, space-charge-limited current (SCLC) measurements were performed using hole-only devices, with an architecture of ITO/PEDOT:PSS/(CsBr)/$CsPbBr_3$/carbon respectively. As depicted in Fig. 4g, the trap fill limit voltage (V_{TFL}) decreased from 1.77 V for the control device to 1.20 V for the CsBr-predeposited device. The N_t was determined using the following equation[6]:

$$N_t = \frac{2\varepsilon\varepsilon_0 V_{TFL}}{eL^2} \#Eq.(3)$$

where ε denoted the dielectric constant of the perovskite, ε_0 represented the vacuum dielectric constant, e signified the elementary charge, and L referred to the thickness of the perovskite layer[42,43]. The lower V_{TFL} and the correspondingly reduced N_t demonstrate that CsBr pre-deposition effectively diminishes the population of electrically active trap states within the $CsPbBr_3$ film. Further insight into parasitic charge loss was obtained from the logarithmic dark *J-V* characteristics presented in Fig. 4h. Compared with the control device, the CsBr-predeposited device exhibited a markedly lower leakage-current density throughout the measured voltage range. This attenuation of dark current suggests that shunt-related conduction pathways and defect-assisted carrier loss are effectively restrained with CsBr pre-deposition[44].

Capacitance-voltage (C-V) measurements were subsequently performed under dark conditions. As shown in Fig. 4i, the CsBr pre-deposited device exhibited a lower capacitance than the control device, consistent with diminished charge accumulation at the $CsPbBr_3/SnO_2$ interface[45]. This behavior can be associated with more effective interfacial electron extraction.

3.5 Charge-transport and recombination kinetics in devices

Moreover, the Mott-Schottky (M-S) plots in Fig. 5a revealed that CsBr pre-deposition increased the built-in potential (V_{bi}) from 1.22 to 1.48 V. The strengthened built-in electric field provides a greater driving force for carrier separation and extraction while mitigating interfacial carrier accumulation[46]. These improvements support the reduced recombination losses and contribute to the enhanced V_{OC} and FF. Fill-factor losses were further evaluated relative to the Shockley-Queisser (S-Q) limit. For a $CsPbBr_3$ bandgap of approximately 2.35 eV, the corresponding S-Q-limited fill factor ($FF_{S\text{-}Q}$) is 0.931[11]. The maximum FF (FF_{max}) was calculated using the following equation:

$$FF_{max} = \frac{\nu_{oc} - \ln(\nu_{oc} + 0.72)}{\nu_{oc} + 1}, \nu_{oc} = \frac{qV_{OC}}{nkT} \#Eq.(4)$$

where q represented the elementary charge, k was the Boltzmann constant, and T denoted the temperature. FF_{max} increased from 0.852 for the control device to 0.878 after CsBr pre-deposition while the corresponding measured values (FF_{mea}) rose from 0.7632 to 0.8074. As depicted in Fig. S11, the gaps between $FF_{S\text{-}Q}$ and FF_{max} as well as FF_{max} and FF_{mea} both narrowed, signifying the simultaneous mitigation of recombination-related and charge-transport-related FF losses.

Transient photovoltage (TPV) and transient photocurrent (TPC) measurements were subsequently employed to interrogate carrier dynamics. As shown in Fig. 5b, the TPV decay lifetime is prolonged from 4.92 to 6.24 ms after CsBr pre-deposition, indicating slower carrier recombination. Conversely, the TPC decay time decreased from 12.86 to 11.43 μs (Fig. 5c), evidencing accelerated charge extraction[47,48]. The extended recombination lifetime and expedited carrier collection jointly account for the gains in V_{OC}, J_{SC}, and FF, thereby supporting the enhanced device efficiency.

Light-intensity-dependent V_{OC} measurements were further conducted to elucidate the dominant recombination pathway. As expressed by the following relationship, the ideality factor (n) was extracted from the slope of V_{OC} versus $\ln(I)$[49]:

$$V_{OC} = \frac{nkT}{q}\ln(I) + C \#Eq.(5)$$

where k represented the Boltzmann constant, q denoted the elementary charge, T indicated the absolute temperature (273 K), and C was a constant. The linear fits in Fig. 5d yielded an n value of 1.966 for the control device, which decreased to 1.649 after CsBr pre-deposition. The shift toward unity signifies a diminished contribution from trap-assisted Shockley-Read-Hall recombination, consistent with the reduced voltage loss and elevated V_{OC} of the modified device[50].

The dependence of J_{SC} on incident-light intensity was subsequently examined to assess bimolecular recombination and carrier-collection behavior. As shown in Fig. 5e, the data were fitted according to the power-law relationship[51]:

$$J_{SC} \propto I^{\alpha} \#Eq.(6)$$

where I denoted the incident-light intensity and α was the power-law exponent. The CsBr-predeposited device exhibited an α value closer to unity than the control device, demonstrating weaker bimolecular recombination and reduced carrier-collection losses under short-circuit conditions[52]. The resulting improvement in photogenerated-carrier collection contributes to the enhanced J_{SC} and overall device performance.

Finally, Fig. 5f demonstrated that the devices with CsBr pre-deposition reserved over 80% of their initial PCE after 1000 h of testing, whereas the control devices fall below this threshold. The remaining photovoltaic parameters displayed a comparable evolution, confirming the slower performance degradation of the modified devices. This enhanced durability can be associated with the improved $CsPbBr_3$ film quality and reduced defect-mediated losses at the buried $SnO_2/CsPbBr_3$ interface, which collectively mitigate device degradation during aging. Overall, Table S6 illustrates the performance of the single-junction all-inorganic $CsPbBr_3$ perovskite solar cells reported in the literature and contrasts them with the parameters of the champion device in this study.

Just Accepted

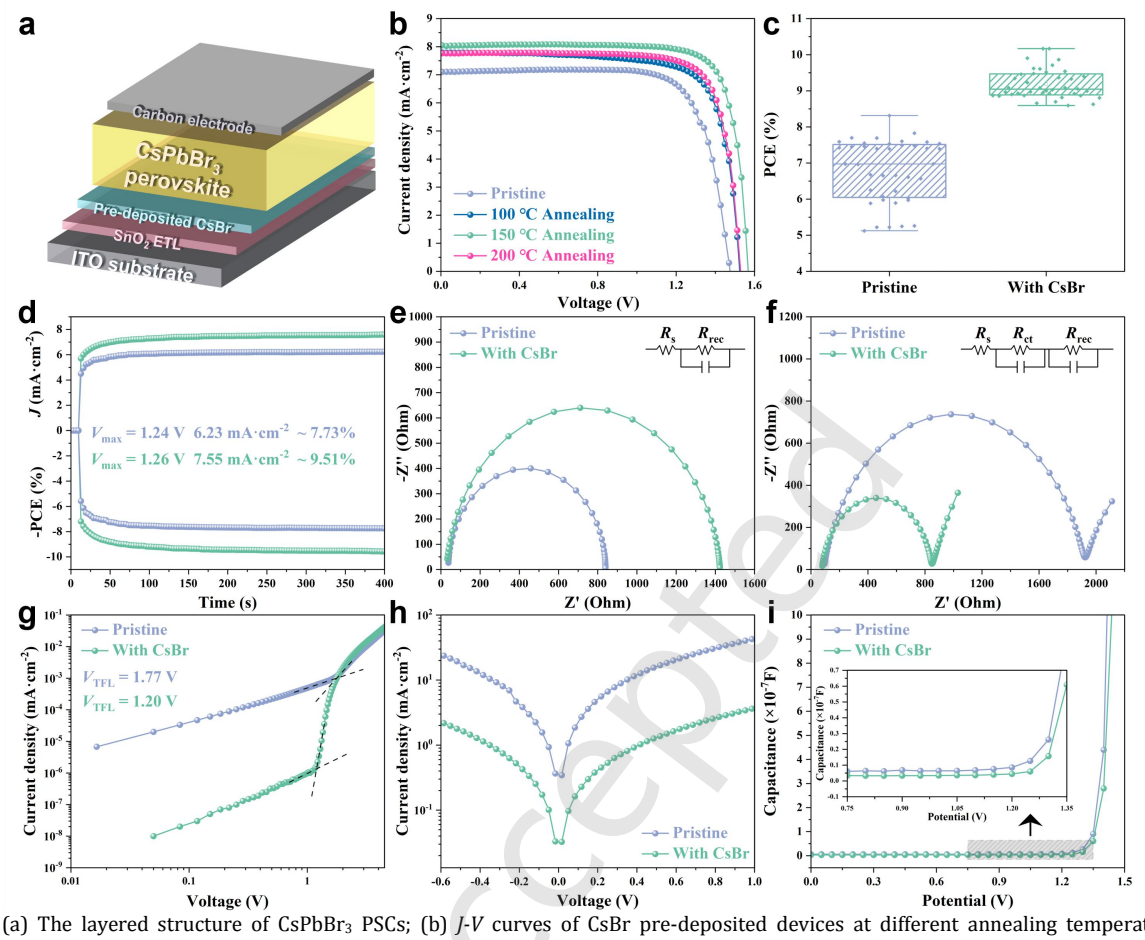


Figure 4 (a) The layered structure of $CsPbBr_3$ PSCs; (b) *J-V* curves of CsBr pre-deposited devices at different annealing temperatures; (c) Statistics of PCE distribution; (d) Steady-state output curves; Nyquist curves in (e) dark environment and (f) under one sunlight illumination, (g) hole-only SCLC curves, (h) logarithmic dark *J-V* curves and (i) C-V curves of devices with or without CsBr.

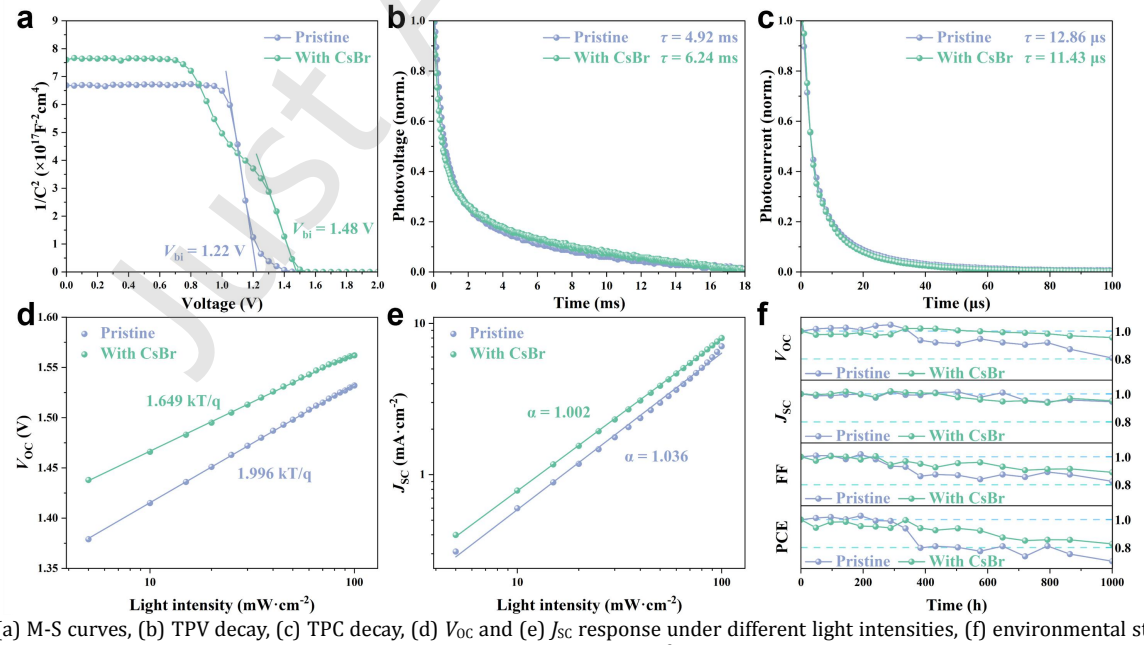


Figure 5 (a) M-S curves, (b) TPV decay, (c) TPC decay, (d) V_{OC} and (e) J_{SC} response under different light intensities, (f) environmental stability of devices with or without CsBr (Room temperature, 40 RH%, AM 1.5 G 100 mW·cm^{-2} solar illumination, without encapsulation, storage in ambiet air condition).

Just Accepted

4 Conclusions

In summary, a CsBr/$PbBr_2$/CsBr sandwich-precursor architecture was developed by introducing a CsBr underlayer between SnO_2 and $PbBr_2$. The buried CsBr layer reshaped the $PbBr_2$ precursor morphology and initiated early-stage interfacial conversion, thereby promoting more homogeneous $CsPbBr_3$ formation and reducing the amount of residual the lead-rich $CsPb_2Br_5$ phase and cesium-rich Cs_4PbBr_6 phase in the final film. Concurrently, it modified the local chemical environment and energy-level alignment of SnO_2, resulting in fewer trap-mediated losses, suppressed nonradiative recombination, and more efficient electron extraction. Benefiting from these coordinated effects, the hole-transport-layer-free carbon-electrode device achieved a champion PCE of 10.12% with a V_{OC} of 1.57 V, markedly outperforming the 7.98% of control device. Moreover, the unencapsulated modified devices retained more than 80% of their initial efficiency after 1000 h of ambient storage. These findings establish buried precursor-architecture engineering as a simple and effective approach for simultaneously regulating phase evolution and interfacial charge dynamics in $CsPbBr_3$ solar cells.

Acknowledgements

This work was supported by the Natural Science Foundation of China (Nos. 61804058, U1705256, 21771066 and 51972123), and thanks for the Instrumental Analysis Center of Huaqiao University.

Declaration of conflicting interests

The authors declare no conflicting interests regarding the content of this article.

Data availability

All data needed to support the conclusions in the paper are presented in the manuscript and/or the Supplementary Materials. Additional data related to this paper may be requested from the corresponding author upon request.

Electronic Supplementary Material: Supplementary material (further details of the XPS spectra, schematic diagram of phase transition in the reaction process, UV–vis spectra of SnO_2 and grain size distribution) is available in the online version of this article at https://doi.org/10.26599/NRE.2026.9120295.

References

[1] Duan, J. L.; Zhao, Y. Y.; He, B. L.; Tang, Q. W. High - purity inorganic perovskite films for solar cells with 9.72% efficiency. *Angew. Chem. Int. Ed.* **2018**, *57*, 3787-3791.

[2] Zhu, J. W.; He, B. L.; Wang, M. X.; Yao, X. P.; Huang, H.; Chen, C.; Chen, H. Y.; Duan, Y. Y.; Tang, Q. W. Elimination of defect and strain by functionalized CQDs dual-engineering for all-inorganic HTMs-free perovskite solar cells with an ultrahigh voltage of 1.651 V. *Nano Energy* **2022**, *104*, 107920.

[3] Zhu, J. W.; He, B. L.; Zhang, W. Y.; Tui, R.; Chen, H. Y.; Duan, Y. Y.; Huang, H.; Duan, J. L.; Tang, Q. W. Defect - dependent crystal plane control on inorganic $CsPbBr_3$ film by selectively anchoring (Pseudo -) halide anions for 1.650 V voltage perovskite solar cells. *Adv. Funct. Mater.* **2022**, *32*, 2206838.

[4] National Renewable Energy Laboratory. *NREL Best Research-Cell Efficiency Chart* [Online]. https://www.nlr.gov/pv/cell-efficiency (accessed August 27, 2026).

[5] Kojima, A.; Teshima, K.; Shirai, Y.; Miyasaka, T. Organometal halide perovskites as visible-light sensitizers for photovoltaic cells. *J. Am. Chem. Soc.* **2009**, *131*, 6050-6051.

[6] Tong, A. L.; Chen, X. H.; Jin, Z. H.; Wang, Y. H.; Zheng, Q. S.; Zhu, W. H.; Sun, W. H.; Wu, J. H. The overlooked hole transport properties of indene-C_{60} bisadduct in $CsPbBr_3$ perovskite solar cells. *Chem. Eng. J.* **2025**, 167567.

[7] Goldschmidt, V. Crystal structure and chemical correlation. *Ber. Dtsch. Chem. Ges.* **1927**, *60*, 1263-1296.

[8] Yuan, Y., Yan, G. H.; Hong, R. J.; Liang, Z. C.; Kirchartz, T. Quantifying efficiency limitations in all - inorganic halide perovskite solar cells. *Adv. Mater.* **2022**, *34*, 2108132.

[9] Tong, G. Q.; Ono, L. K.; Qi, Y. B. Recent progress of all - bromide inorganic perovskite solar cells. *Energy Technol.* **2020**, *8*, 1900961.

[10] Ullah, S.; Wang, J. M.; Yang, P. X.; Liu, L. L.; Yang, S.-E.; Xia, T. Y.; Guo, H. Z.; Chen, Y. S. All-inorganic $CsPbBr_3$ perovskite: a promising choice for photovoltaics. *Mater. Adv.* **2021**, *2*, 646-683.

[11] Rühle, S. Tabulated values of the Shockley–Queisser limit for single junction solar cells. *Sol. Energy* **2016**, *130*, 139-147.

[12] Zhou, Q. W.; Duan, J. L.; Du, J., Guo, Q. Y.; Zhang, Q. Y.; Yang, X. Y.; Duan, Y. Y.; Tang, Q. W. Tailored lattice “tape” to confine tensile interface for 11.08% - efficiency all - inorganic $CsPbBr_3$ perovskite solar cell with an ultrahigh voltage of 1.702 V. *Adv. Sci.* **2021**, *8*, 2101418.

[13] Kulbak, M.; Cahen, D.; Hodes, G. How important is the organic part of lead halide perovskite photovoltaic cells? Efficient $CsPbBr_3$ cells. *J. Phys. Chem. Lett.* **2015**, *6*, 2452-2456.

[14] Liang, K. B.; Zhang, Y. Y.; Wang, C. H.; Hua, G. X.; Yang, W. D.; Jin, Y. N.; Zhang, C. H.; Chen, S. T.; Zhu, C. W.; Sun, W. H. Effects of DMSO vapor-assisted annealing on the performance of $CsPbBr_3$ perovskite solar cells. *Chin. Sci. Bull.* **2023**, *68*, 1689-1698.

[15] Shao, W.; Sheng, J.; Fu, Y. F.; He, J. W.; Deng, Z. H.; Cen, R. H.; Wu, W. J. Achieving unprecedented power-output in 4-terminal mirror-symmetrical printable carbon $CsPbBr_3$ solar cells through dual-solvent engineering. *Energy Environ. Sci.* **2025**, *18*, 3211-3222.

[16] Lee, S. K.; Bark, C. W. Dispersed SnO_2 colloids using sodium dodecyl benzene sulfonate for high-performance planar perovskite solar cells. *Sol. Energy* **2021**, *230*, 747-753.

[17] Hu, W. P.; Yang, S. F.; Yang, S. H. Surface modification of TiO_2 for perovskite solar cells. *Trends Chem.* **2020**, *2*, 148-162.

[18] Yan, H. L.; Zhao, X.; Huang, H.; Wu, D. X.; Zhu, P. K.; Li, D. N.; Fan, B. B.; Qiu, Y. J.; Yang, Y. Q.; Geng, Q. Flocculating - regulated TiO_2 deposition enables the synergistic effect of doping for perovskite solar cells with efficiency exceeding 25.8%. *Adv. Energy Mater.* **2025**, *15*, 2403200.

[19] Zhao, W. H.; Guo, P. F.; Wu, J. H.; Lin, D. Y.; Jia, N.; Fang, Z. Y.; Liu, C.; Ye, Q.; Zou, J. J.; Zhou, Y. Y. TiO_2 electron transport layer with p–n homojunctions for efficient and stable perovskite solar cells. *Nano-Micro Lett.* **2024**, *16*, 191.

[20] Li, Z. S.; Wang, Y. C.; Wang, Y. J.; Zhu, W. H.; Yin, X. Y.; Yang, W. D.; Zheng, S. Z.; Sun, W. H. Preparation of $CsPbBr_3$

Just Accepted

perovskite solar cells via bottom interface modification with methylammonium chloride. *Chin. J. Inorg. Chem.* **2025**, *41*,

[21] Zhang, X. H.; Ye, J. J.; Zhu, L. Z.; Zheng, H. Y.; Liu, G. Z.; Liu, X. P.; Duan, B.; Pan, X.; Dai, S. Y. High-efficiency perovskite solar cells prepared by using a sandwich structure MAI–PbI_2–MAI precursor film. *Nanoscale* **2017**, *9*, 4691-4699.

[22] Xiao, Y. D.; Cui, X. Q.; Xiang, B. Y.; Chen, Y. P.; Zhao, C. Y.; Wang, L. H.; Yang, C. Q.; Zhang, G. Y.; Xie, C.; Han, Y. L. $MDACl_2$-modified SnO_2 film for efficient planar perovskite solar cells. *Molecules* **2023**, *28*, 2668.

[23] Li, H.; Wang, Z. Y.; Zheng, S. Z.; Zhu, W. H.; Zhang, Y. Y.; Wang, Y.; Sun, W. H.; Wu, J. H. Surface defects manipulation of TiO_2 ETL for $CsPbBr_3$ perovskite solar cells via introducing TMAH molecular layer. *Surf. Interfaces* **2025**, *62*, 106255.

[24] Belarbi, E.; Vallés-Pelarda, M.; Clasen Hames, B.; Sanchez, R. S.; Barea, E. M.; Maghraoui-Meherzi, H.; Mora-Seró, I. Transformation of PbI_2, $PbBr_2$ and $PbCl_2$ salts into $MAPbBr_3$ perovskite by halide exchange as an effective method for recombination reduction. *Phys. Chem. Chem. Phys.* **2017**, *19*, 10913-10921.

[25] Jin, Z. H.; Tong, A. L.; Wang, Y. H.; Yin, X. Y.; Wang, Y.; Chen, X. H.; Sun, W. H.; Fu, C. P.; Wu, J. H. Development of a CsBr/MeOH antisolvent dropping strategy for enhanced performance of $CsPbBr_3$ perovskite solar cells. *Mater. Today Chem.* **2025**, *47*, 102784.

[26] Liang, K. B.; Wu, Y. J.; Zheng, Q. S.; Zou, Y.; Zhang, X. C.; Wang, C. H.; Shi, P. Y.; Zhang, Y. Y.; Sun, W. H.; Li, Y. L. Solvent vapor annealing-assisted mesoporous $PbBr_2$ frameworks for high-performance inorganic $CsPbBr_3$ perovskite solar cells. *Surf. Interfaces* **2023**, *37*, 102707.

[27] Wang, Y.; Tong, A. L.; Wang, Y. H.; Liang, K. B.; Zhu, W. H.; Wu, Y. J.; Sun, W. H.; Wu, J. H. Interfacial modulation by ammonium salts in hole transport layer free $CsPbBr_3$ solar cells with fill factor over 86%. *Mater. Today Chem.* **2024**, *40*, 102228.

[28] Huang, C. -Y.; Huang, S. -H.; Wu, C. -L.; Wang, Z. -H.; Yang, C. -C. Cs_4PbBr_6/$CsPbBr_3$ nanocomposites for all-inorganic electroluminescent perovskite light-emitting diodes. *ACS Appl. Nano Mater.* **2020**, *3*, 11760-11768.

[29] Wang, S. B.; Cao, F. X.; Sun, W. H.; Wang, C. Y.; Yan, Z. L.; Wang, N.; Lan, Z.; Wu, J. H. A green Bi-Solvent system for processing high-quality $CsPbBr_3$ films in efficient all-inorganic perovskite solar cells. *Mater. Today Phys.* **2022**, *22*, 100614.

[30] Tong, A. L.; Jin, Z. H.; Chen, X. H.; Zhu, W. H.; Zheng, Q. S.; Wang, Y. H.; Wang, Y.; Ma, N. G.; Sun, W. H.; Fu, C. P. Can fullerene derivative PCBM serve as an innovative hole transport material for $CsPbBr_3$ perovskite solar cells? *Chem. Eng. J.* **2025**, *503*, 158507.

[31] Haris, M. P.; Kazim, S.; Ahmad, S. Microstrain and urbach energy relaxation in $FAPbI_3$-based solar cells through powder engineering and perfluoroalkyl phosphate ionic liquid additives. *ACS Appl. Mater. Interfaces* **2022**, *14*, 24546-24556.

[32] Meng, Q. X.; Feng, J. Y.; Huang, H. T.; Han, X. P.; Zhu, Z.; Yu, T.; Li, Z. S.; Zou, Z. G. Simultaneous optimization of phase and morphology of $CsPbBr_3$ films via controllable Ostwald Ripening by ethylene glycol monomethylether/isopropanol Bi‐Solvent engineering. *Adv. Eng. Mater.* **2020**, *22*, 2000162.

[33] Chen, X. H.; Wang, Z. Y.; Fan, Z.; Li, H.; Zhang, C. H.; Zheng, S. Z.; Zhu, W. H.; Wang, Y.; Sun, W. H.; Wu, J. H. Polymer interface engineering for highly stable $CsPbBr_3$ perovskite solar cells. *Surf. Interfaces* **2025**, 107503.

[34] Zhang, J. S.; Guo, Q. Y.; Zhao, Y. Y.; Duan, J. L.; Tang, Q. W. In situ formation of inorganic healing overlayer for interface-stabilized all-inorganic $CsPbIBr_2$ perovskite solar cells. *Chem. Commun.* **2022**, *58*, 13891-13894.

[35] Numata, Y.; Shibayama, N.; Miyasaka, T. $FAPbBr_3$ perovskite solar cells with V_{OC} values over 1.5 V by controlled crystal growth using tetramethylenesulfoxide. *J. Mater. Chem. A* **2022**, *10*, 672-681.

[36] Xie, G. X.; Lu, X. C.; Duan, J. L.; Dong, Y.; Jiang, X. R.; Tu, F. Z.; Duan, Y. Y.; Tang, Q. W. Alkali chloride doped SnO_2 electron-transporting layers for boosting charge transfer and passivating defects in all-inorganic $CsPbBr_3$ perovskite solar cells. *J. Mater. Chem. A* **2021**, *9*, 15003-15011.

[37] Zhou, L.; Sui, M. J.; Zhang, J. J.; Cao, K.; Wang, H. Q.; Yuan, H. D.; Lin, Z. H.; Zhang, J. C.; Li, P. X.; Hao, Y. Tailored buried layer passivation toward high-efficiency carbon based all-inorganic $CsPbBr_3$ perovskite solar cell. *Chem. Eng. J.* **2024**, *496*, 154043.

[38] Wu, Y. J.; Wang, J. Y.; Zhu, W. H.; Liang, K. B.; Wang, Y.; Chen, X. H.; Sun, W. H.; Fu, C. P. Alkali metal fluoride synergistically passivates the buried interface to achieve high-efficiency and stable all-inorganic $CsPbBr_3$ perovskite solar cells. *Chin. Sci. Bull.* **2025**, *71*, 825-838.

[39] Wang, Y.; Zhu, W. H.; Chen, X. H.; Yang, X. T.; Tong, A. L.; Yang, S.; Wu, J. H.; Sun, W. H. Bulk and surface defect manipulation of the ZnO ETL for all-inorganic $CsPbBr_3$ perovskite solar cells. *Nanoscale* **2025**, *17*, 12299-12309.

[40] Jiao, W. J.; He, B. L.; Wang, Z. Y.; Sun, S. H.; Wei, M.; Liu, W. L.; Sun, M. R.; Chen, H. Y.; Li, H. Y.; Duan, J. L. Reducing oxygen vacancies of MoO_3 by polyaniline functionalization for stable and efficient inorganic tri-brominated perovskite solar cells. *Mater. Today Phys.* **2024**, *46*, 101514.

[41] Bian, L. Q.; Jia, Y.; Zhao, Y. Y.; Dou, Z.; Guo, Q. Y.; Duan, J. L.; Dou, J.; Sun, L. Q.; Zhang, Q.; Tang, Q. W. Target therapy at buried interfaces toward efficient and stable inorganic perovskite solar cells. *Chem. Eng. J.* **2024**, *496*, 154189.

[42] Du, J.; Duan, J. L.; Duan, Y. Y.; Tang, Q. W. Tailoring organic bulk-heterojunction for charge extraction and spectral absorption in $CsPbBr_3$ perovskite solar cells. *Sci. China Mater.* **2021**, *64*, 798-807.

[43] Wang, K.-L.; Wang, R.; Wang, Z.-K.; Li, M.; Zhang, Y.; Ma, H.; Liao, L.-S.; Yang, Y. Tailored phase transformation of $CsPbI_2Br$ films by copper (II) bromide for high-performance all-inorganic perovskite solar cells. *Nano Lett.* **2019**, *19*, 5176-5184.

[44] Rodkey, N.; Zanoni, K. P.; Piot, M.; Dreessen, C.; Grote, R.; Carroy, P.; Sebastian Alonso, J. E.; Paliwal, A.; Muñoz, D.; Bolink, H. J. Efficient micrometer thick bifacial perovskite solar cells. *Adv. Energy Mater.* **2024**, *14*, 2400058.

[45] Tong, A. L.; Zhu, C. W.; Yan, H. Y.; Zhang, C. H.; Jin, Y. N.; Wu, Y. J.; Cao, F. X.; Wu, J. H.; Sun, W. H. Defect control for high-efficiency all-inorganic $CsPbBr_3$ perovskite solar cells via hydrophobic polymer interface passivation. *J. Alloys Compd.* **2023**, *942*, 169084.

[46] Yang, J. M.; Xiong, S. B.; Song, J. N.; Wu, H. B.; Zeng, Y. H.; Lu, L. Y.; Shen, K. C.; Hao, T. Y.; Ma, Z. F.; Liu, F. Energetics and energy loss in 2D Ruddlesden–Popper perovskite solar cells. *Adv. Energy Mater.* **2020**, *10*, 2000687.

[47] Hidayat, R.; Nurunnizar, A. A.; Fariz, A.; Herman, Rosa, E. S.; Shobih, Oizumi, T.; Fujii, A.; Ozaki, M. Revealing the charge carrier kinetics in perovskite solar cells affected by mesoscopic structures and defect states from simple transient photovoltage measurements. *Sci. Rep.* **2020**, *10*, 19197.

[48] Xiong, Z.; Chen, X.; Zhang, B.; Odunmbaku, G. O.; Ou, Z. P.; Guo, B.; Yang, K.; Kan, Z. P.; Lu, S. R.; Chen, S. S. Simultaneous interfacial modification and crystallization control by biguanide hydrochloride for stable perovskite solar cells with PCE of 24.4%. *Adv. Mater.* **2022**, *34*, 2106118.

[49] Duan, J. L.; Zhao, Y. Y.; Wang, Y. D.; Yang, X. Y.; Tang, Q. W. Hole‐boosted Cu(Cr, M)O_2 nanocrystals for all‐inorganic

Just Accepted

$CsPbBr_3$ perovskite solar cells. *Angew. Chem. Int. Ed.* **2019**, *58*, 16147-16151.

[50] Chen, P. X.; Pan, W. C.; Wang, S. B.; Zheng, Q. S.; Tong, A. L.; He, R. W.; Wu, J. H.; Sun, W. H.; Li, Y. L. Enhancing efficiency and stability of perovskite solar cells through methoxyamine hydrochloride modified SnO_2 electron transport layer. *Chem. Eng. J.* **2024**, *488*, 151162.

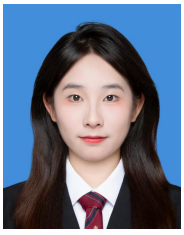
[51] Yan, F. R.; Duan, J. L.; Guo, Q. Y.; Zhang, Q. Y.; Yang, X. Y.; Yang, P. Z.; Tang, Q. W. Solution microcrystal enables a high-quality $CsPbIBr_2$ film to minimize intragranular charge recombination for air-stable, carbon-based photovoltaics. *Sci. China Mater.* **2023**, *66*, 485-492.

[52] He, J. C.; Sheng, W. P.; Yang, J.; Zhong, Y.; Su, Y.; Tan, L. C.; Chen, Y. W. Omnidirectional diffusion of organic amine salts assisted by ordered arrays in porous lead iodide for two-step deposited large-area perovskite solar cells. *Energy Environ. Sci.* **2023**, *16*, 629-640.

Just Accepted



Wenhao Zhu received his B.E. degree from the Materials Science and Engineering, Huaqiao University, in July 2026. He is currently a Master candidate of Energy Storage Science and Engineering, Xi'an Jiaotong University. His research interests focus on all-bromide perovskite photovoltaics, including all-inorganic $CsPbBr_3$ solar cells and $FAPbBr_3$ solar cells.



Minyue Zhang entered the Engineering Center of Environmental Friendly Functional Materials of the Ministry of Education in 2025. It is the third year of undergraduate study in the School of Materials Science and Engineering of Huaqiao University. Her research interests are novel functional materials and novel photovoltaic devices.



Yang Wang received his bachelor's degree in Polymer Materials and Engineering in 2025 and graduated from Huaqiao University. His research focuses on the carbon-based hole-transport-layer-free all-inorganic $CsPbBr_3$ perovskite solar cells.



Yunjia Wu received his B.E. degree from Huaqiao University and his M.E. degree from Xiamen University. His research focuses on perovskite photovoltaics, particularly molecular interface engineering, self-assembled monolayers, buried-interface modulation, and defect passivation. He also has experience in all-inorganic $CsPbBr_3$ solar cells and scalable perovskite device processing.



Chen Yang received her Ph.D. degree from King Abdullah University of Science and Technology (KAUST) in 2022. She is currently a researcher at the Xinjiang Technical Institute of Physics and Chemistry, Chinese Academy of Sciences. Her research focuses on high-efficiency and stable perovskite solar cells, silicon–perovskite tandem photovoltaics, large-area module processing, and photovoltaic-driven hydrogen production.



Weihai Sun is an associate professor at Engineering Research Center of Environment-Friendly Functional Materials, Ministry of Education, School of Materials Science and Engineering, Huaqiao University, China. He obtained his PhD degree in the College of Chemistry and Molecular Engineering, Peking University in 2015. Thereafter, he worked as postdoctoral fellow with Prof. Zhijian Chen and Lixin Xiao in the State Key Laboratory for Mesoscopic Physics and Department of Physics, Peking University. His main research focuses on optoelectronic materials and devices.



Jihuai Wu is Professor in Chemistry and Materials, and was the vice-president (2004–2019) at Huaqiao University, China. He obtained his master's degree in Materials in 1988 from Huaqiao University, China, and obtained his PhD degree in Chemistry in 1999 from Fuzhou University, China. His main research focuses on photo-electronic functional materials and devices, superabsorbent polymers, photocatalytic intercalated nanomaterials, especially dye-sensitized solar cells and perovskite solar cells. He has published more than 500 scientific articles. He is Elsevier's Most Cited Chinese Researcher, RSC's Top 1% Highly-Cited Chinese Author, and Clarivate's (Web of Science) Highly Cited Researcher

Just Accepted

Electronic Supplementary Material

$CsBr/PbBr_2/CsBr$ sandwich-precursor deposition suppresses secondary phases in $CsPbBr_3$ solar cells

Wenhao Zhu[1,§], Minyue Zhang[1,§], Yang Wang[1,§], Chenwei Zhu[1], Yinuo Jin[1], Chunhong Zhang[1], Shaotian Chen[1], Shiying Sun[2,3], Yunjia Wu[1](✉), Chen Yang[2,3](✉), Weihai Sun[1](✉), and Jihuai Wu[1](✉)

[1] *Engineering Research Center of Environment-Friendly Functional Materials, Ministry of Education, College of Materials Science and Engineering, Huaqiao University, Xiamen 361021, China.*
[2] *Research Center for Energy and Chemical Engineering, Xinjiang Technical Institute of Physics and Chemistry, Chinese Academy of Sciences, Urumqi, 830011, China.*
[3] *University of Chinese Academy of Sciences (UCAS), Beijing, 100049, China.*
[§] *Wenhao Zhu, Minyue Zhang and Yang Wang contributed equally to this work.*

Supporting information to https://doi.org/10.26599/NRE.2026.9120295

Figures S1~S11



Figure S1 Physical imagine of the device with CsBr pre-deposition.

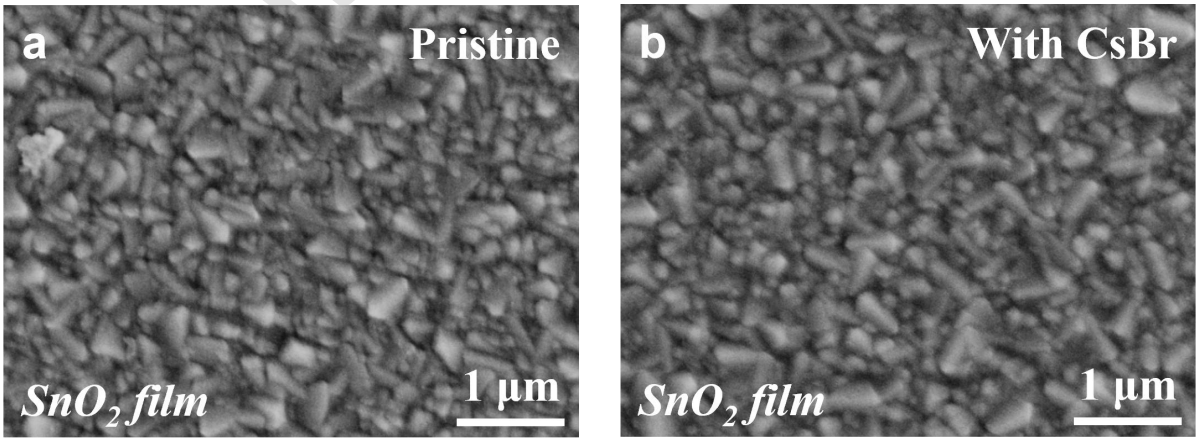


Figure S2 SEM images of (a) pristine SnO_2 films and (b) SnO_2 films with CsBr pre-deposition.

Just Accepted

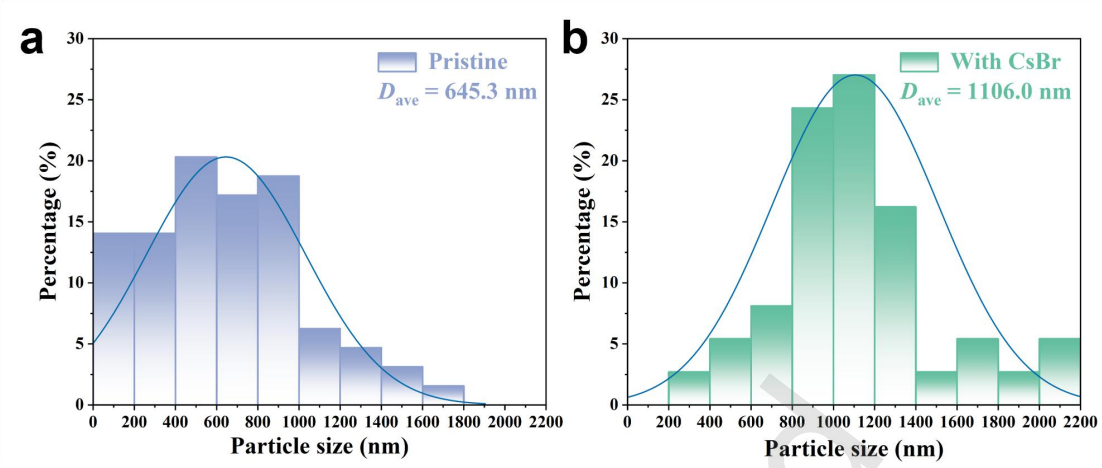


Figure S3 Grain size distribution of (a) pristine PVK films and (b) PVK films with CsBr pre-deposition.

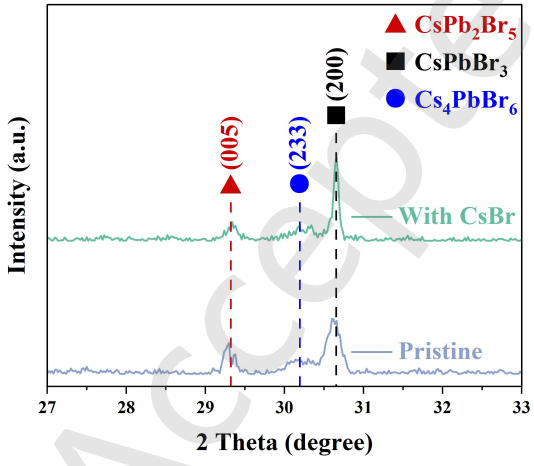


Figure S4 Enlarged XRD patterns for PVK films at 27–33 degrees with or without CsBr pre-deposition.

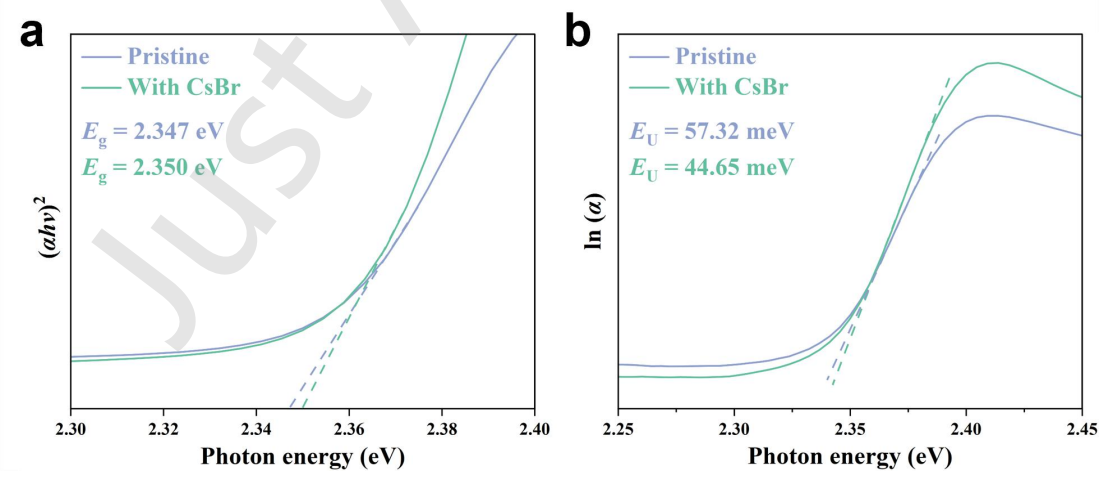


Figure S5 (a) Tauc plots and (b) Urbach energy of PVK films with or without CsBr pre-deposition.

Just Accepted

Address correspondence to Jihuai Wu, jhwu@hqu.edu.cn; Weihai Sun, sunweihai@hqu.edu.cn; Chen Yang, yangchen@ms.xjb.ac.cn; Yunjia Wu, wuyunjia@stu.hqu.edu.cn

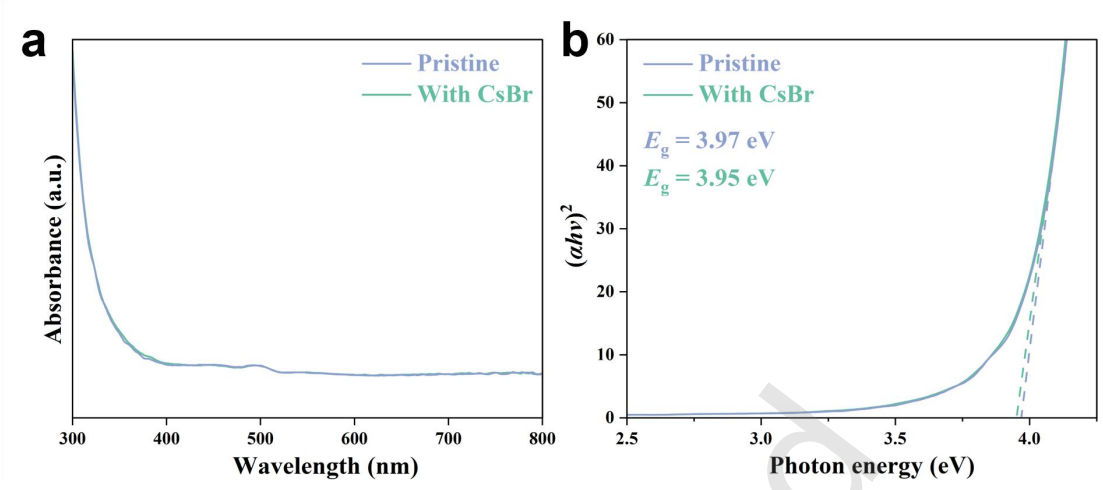


Figure S6 (a) UV–vis spectra and (b) Tauc plots of SnO_2 films with or without CsBr pre-deposition.

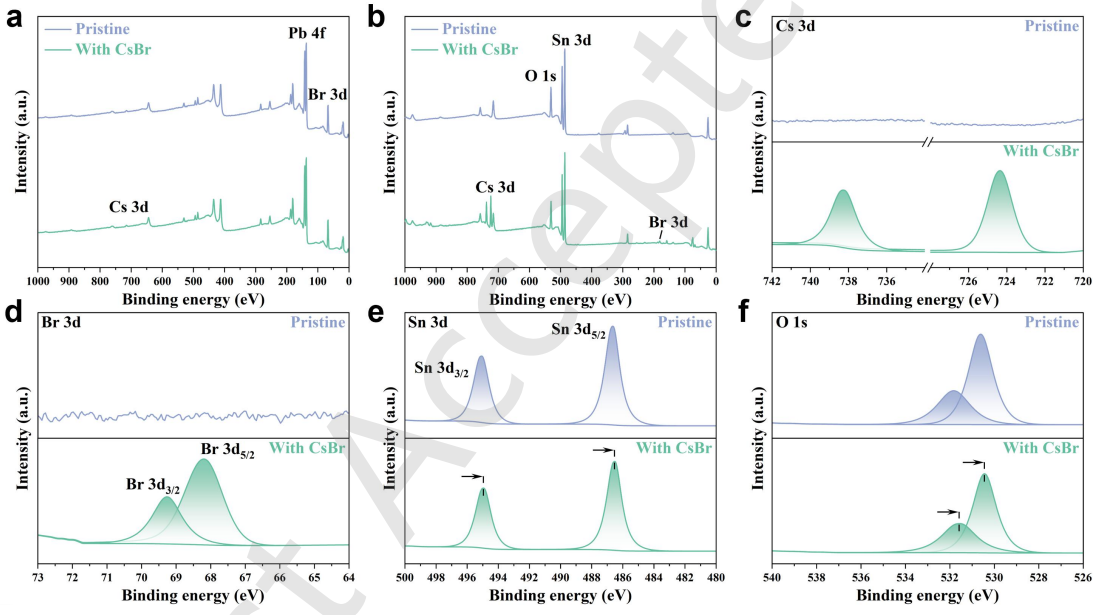


Figure S7 The complete XPS spectra of (a) $PbBr_2$ films and (b) SnO_2 films with or without CsBr pre-deposition; The corresponding high-resolution XPS spectra of (c) Cs 3d, (d) Br 3d, (e) Sn 3d, and (f) O 1s for SnO_2 films with or without CsBr pre-deposition.

Just Accepted

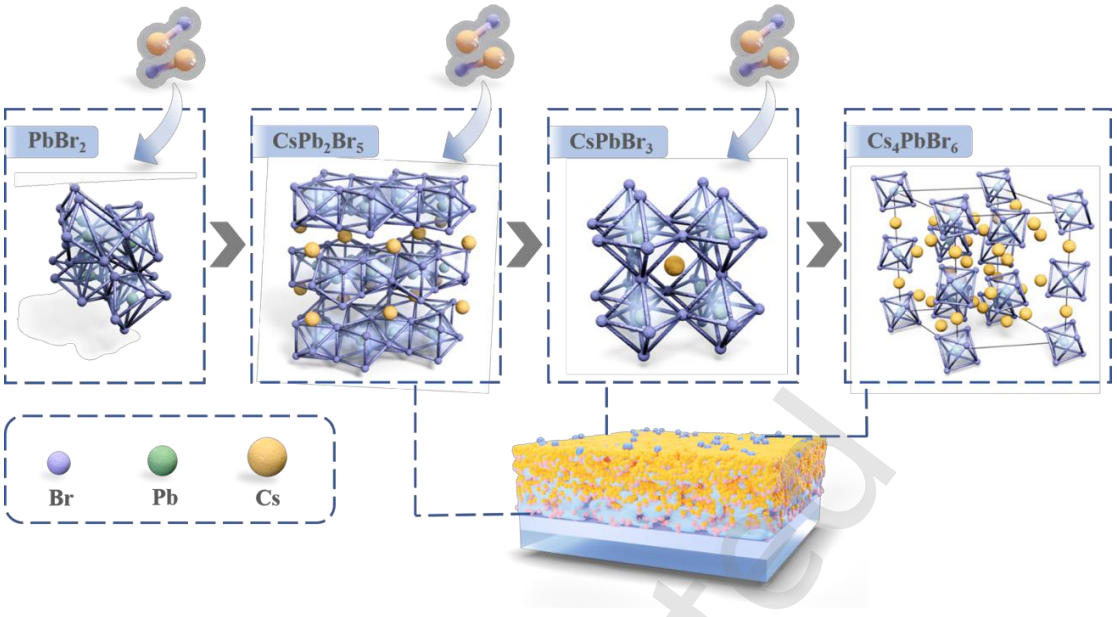


Figure S8 Schematic diagram of phase transition in the reaction process between $PbBr_2$ and CsBr.

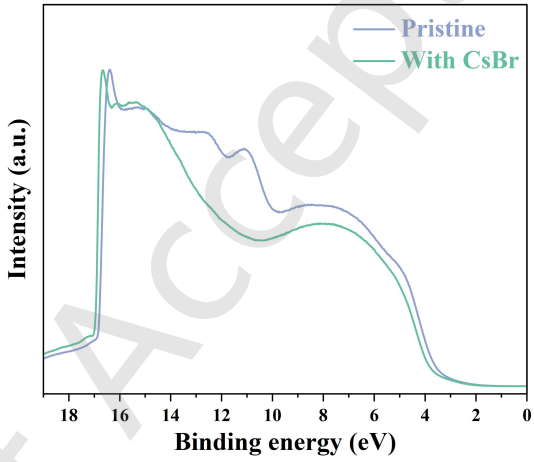


Figure S9 UPS spectra of secondary-electron cut-off edge of SnO_2 films with or without CsBr pre-deposition.

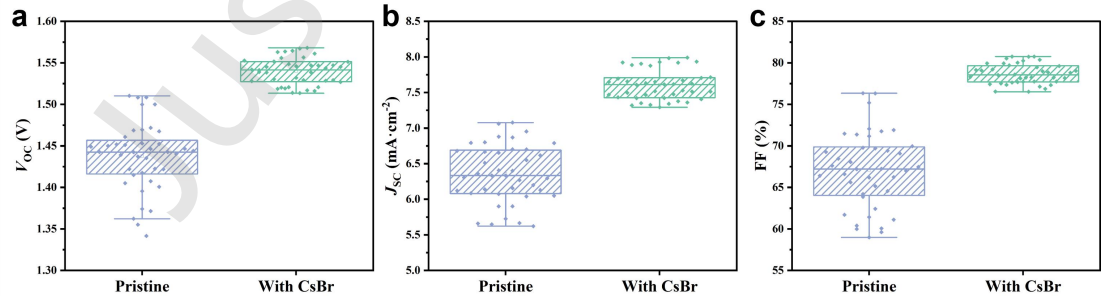


Figure S10 Statistics of (a)V_{OC}, (b) J_{SC} and (c) FF distribution of devices with or without CsBr pre-deposition.

Just Accepted

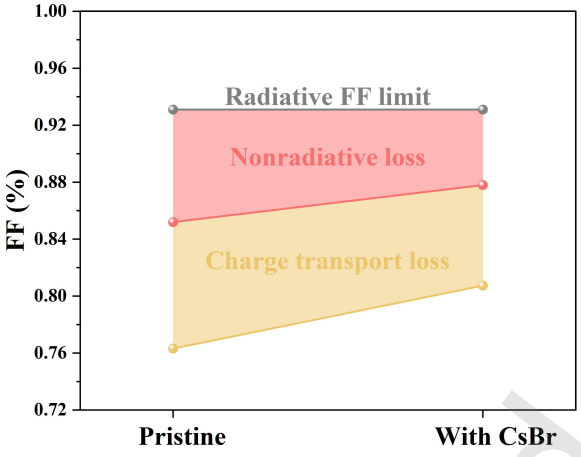


Figure S11 FF_{S-Q} limit diagram.

Just Accepted

Tables S1~S6

Table S1 TRPL data of PVK films with or without CsBr pre-deposition.

Sample	τ_{ave} (ns)	A_1 (%)	τ_1 (ns)	A_2 (%)	τ_2 (ns)
Pristine	7.50	74.42	1.11	25.58	9.70
With CsBr	10.20	69.27	1.64	30.73	13.99

Table S2 The calculated values of energy level of SnO_2 films with and without CsBr pre-deposition.

Sample	E_{cutoff} (eV)	E_{onset} (eV)	E_F (eV)	E_{VB} (eV)	E_{CB} (eV)	E_g (eV)
Pristine	16.81	3.56	-4.41	-7.97	-3.99	3.97
With CsBr	16.95	3.63	-4.27	-7.90	-3.95	3.95

Table S3 Photovoltaic data statistics of 40 pristine devices and 40 devices with CsBr pre-deposition.

Sample	Data	V_{OC} (V)	J_{SC} (mA·cm^{-2})	FF (%)	PCE (%)
Pristine	Champion	1.47	7.11	76.32	7.98
	Average	1.44 ± 0.04	6.35 ± 0.41	67.05 ± 4.58	6.81 ± 0.87
With CsBr	Champion	1.57	7.98	80.74	10.12
	Average	1.53 ± 0.02	7.60 ± 0.21	78.67 ± 1.21	9.18 ± 0.41

Just Accepted

Table S4 Electrical impedance data of devices with and without CsBr pre-deposition in dark environment.

Sample	R_s (Ω)	R_{rec} (Ω)
Pristine	37.37	802
With CsBr	27.56	1396

Table S5 Electrical impedance data of devices with and without CsBr pre-deposition under one sun illumination.

Sample	R_s (Ω)	R_{ct} (Ω)	R_{rec} (Ω)
Pristine	88.66	1464	1832
With CsBr	77.31	768.3	3365

Table S6 Summary table of the n-i-p structure devices with the same perovskite composition published in recent years.

Device structure	V_{OC} (V)	J_{SC} (mA·cm^{-2})	FF (%)	PCE (%)	Reference	Year
FTO/TiO_2/EGME-$CsPbBr_3$/Carbon	1.51	7.48	84.49	9.55	[1]	2022
FTO/c-TiO_2/m-TiO_2/Br-CQDs/$CsPbBr_3$+Br-CQDs/Carbon	1.651	7.84	83.36	10.79	[2]	2022
FTO/TiO_2/DMF-$CsPbBr_3$/Carbon	1.54	7.57	82.37	9.60	[3]	2023
FTO/TiO_2/$CsPbBr_3$/BABr/Carbon	1.55	7.39	86.10	9.86	[4]	2024
ITO/SnO_2/KI-$CsPbBr_3$/Carbon	1.60	7.65	82.23	10.06	[5]	2025
FTO/SnO_2 QDs/TiO_xCl_{4-2x}/$CsPbBr_3$/Carbon	1.707	7.88	83.48	11.23	[6]	2025
FTO/SnO_2-TiO_xCl_{4-2x}/DOP-BTA-$CsPbBr_3$/Carbon	1.741	7.92	81.25	11.20	[7]	2026
ITO/CsBr-SnO_2/$CsPbBr_3$/Carbon	1.57	7.98	80.74	10.12	This work	2026

Just Accepted

References

[1] Wang, S. B.; Cao, F. X.; Sun, W. H.; Wang, C. Y.; Yan, Z. L.; Wang, N.; Lan, Z.; Wu, J. H. A green Bi-Solvent system for processing high-quality $CsPbBr_3$ films in efficient all-inorganic perovskite solar cells. *Mater. Today Phys.* **2022**, *22*, 100614.

[2] Zhu, J. W.; He, B. L.; Wang, M. X.; Yao, X. P.; Huang, H.; Chen, C.; Chen, H. Y.; Duan, Y. Y.; Tang, Q. W. Elimination of defect and strain by functionalized CQDs dual-engineering for all-inorganic HTMs-free perovskite solar cells with an ultrahigh voltage of 1.651 V. *Nano Energy* **2022**, *104*, 107920.

[3] Liang, K. B.; Wu, Y. J.; Zheng, Q. S.; Zou, Y.; Zhang, X. C.; Wang, C. H.; Shi, P. Y.; Zhang, Y. Y.; Sun, W. H.; Li, Y. L. Solvent vapor annealing-assisted mesoporous $PbBr_2$ frameworks for high-performance inorganic $CsPbBr_3$ perovskite solar cells. *Surf. Interfaces* **2023**, *37*, 102707.

[4] Wang, Y.; Tong, A. L.; Wang, Y. H.; Liang, K. B.; Zhu, W. H.; Wu, Y. J.; Sun, W. H.; Wu, J. H. Interfacial modulation by ammonium salts in hole transport layer free $CsPbBr_3$ solar cells with fill factor over 86%. *Mater. Today Chem.* **2024**, *40*, 102228.

[5] He, R. W.; Wu, Y. J.; Li, Z.; Wang, Y.; Zhu, W. H.; Tong, A. L.; Chen, X. H.; Pan, W. C.; Sun, W. H.; Wu, J. H. Bulk and interface passivation through potassium iodide additives engineering enables high-performance and humidity-stable $CsPbBr_3$ perovskite solar cells. *Surf. Interfaces* **2024**, *48*, 104274.

[6] Teng, Y. P.; Zhao, Y. Y.; Xin, Z.; Bian, L. Q.; Guo, Q. Y.; Duan, J. L.; Dou, J.; Zhang, Y.; Zhang, Q.; Tang, Q. W. Dual-site synergistic passivation for $CsPbBr_3$ perovskite solar cells with record 1.707 V V_{OC} and 11.23% efficiency. *J. Mater. Chem. A* **2025**, *13*, 21493.

[7] Tang, W. H.; Zhao, Y. Y.; Shen, L. N.; Yang, M. Y.; Wang, Q. R.; Duan, J. L.; Dou, J.; Guo, Q. Y.; He, B. L.; Zhang, Q.; Zhang, Y.; Tang, Q. W. Crosslinking-induced chelation and stress compression for high-efficiency all-inorganic $CsPbBr_3$ perovskite solar cells. *Adv. Funct. Mater.* **2026**, *36*, e77137.

Just Accepted